RSC Advances

PAPER

View Article Online
View Journal | View Issue

Cite this: *RSC Adv.*, 2018, **8**, 17139

Frequency and temperature-dependence of dielectric permittivity and electric modulus studies of the solid solution $Ca_{0.85}Er_{0.1}Ti_{1-x}Co_{4x/3}O_3$ ($0 \leq x \leq 0.1$)

Ch. Rayssi, *[a] S. El.Kossi,[a] J. Dhahri [a] and K. Khirouni[b]

Received 25th January 2018
Accepted 27th April 2018

DOI: 10.1039/c8ra00794b

rsc.li/rsc-advances

The dielectric properties of $Ca_{0.85}Er_{0.1}Ti_{1-x}Co_{4x/3}O_3$ ($CETCo_x$) ($x = 0.00$, 0.05 and 0.10), prepared by a sol–gel method, were systematically characterized. The temperature and frequency dependence of the dielectric properties showed a major effect of the grain and grain boundary. The dielectric constant and dielectric loss of $CETCo_x$ decreased sharply with increasing frequency. This is referred to as the Maxwell–Wagner type of polarization in accordance with Koop's theory. As a function of temperature, the dielectric loss and the real part of permittivity decreased with increasing frequency as well as Co rate. Indeed, a classical ferroelectric behavior was observed for $x = 0.00$. The non-ferroelectric state of the grain boundary and its correlation with structure, however, proved the existence of a relaxor behavior for $x = 0.05$ and 0.10. The complex electric modulus analysis $M^*(\omega)$ confirmed that the relaxation process is thermally activated. The normalized imaginary part of the modulus indicated that the relaxation process is dominated by the short range movement of charge carriers.

1. Introduction

Perovskite-based ferroelectric materials with the ABO_3 chemical formula have been studied owing to their physical properties and their important applications in functional technologies such as actuators, sensors, memories (FRAM), capacitors, micro-electromechanical systems, energy harvesting[1] and more recently in opto-electronic devices.[2] ABO_3 perovskites are the most important materials for piezoelectric, dielectric, ferroelectric and pyroelectric applications.[3,4] Relaxor ferroelectric materials are characterized by a high frequency dispersion of dielectric permittivity where the maximum value of the temperature (T_m) of the dielectric constant shifts to higher temperatures and frequencies. The relaxor behavior is usually explained by many theoretical models, such as order-disorder model, micro–macro domain transitions model and dipole inhomogeneity model, as well as certain phenomena such as local random field, dipolar glass and supra-electricity.[5,6] $CaTiO_3$ belongs to a class of attractive materials thanks to their technological properties such as ferroelectricity, electro-mechanical-optical conversion, and photoluminescence.[7] Due to its properties, $CaTiO_3$ offers a wide range of technological applications and it can be used as a dielectric resonator in wireless communication systems[8–10] and photocatalysts or of immobilizing nuclear waste, luminescent (light emitting) devices[11–13] and biomaterials.[14] Owing to their applications in the miniaturization of electronic devices, the dielectric materials with a high value of dielectric constant (ε') have recently attracted much attention.[15] The high permittivity (ε') and low dielectric loss ($\tan\delta$) of $CaTiO_3$ make it suitable for microwave dielectric applications as filters and resonators.[16,17] From the X-ray diffraction, it was observed that calcium titanate ($CaTiO_3$) has a distorted orthorhombic structure. At room temperature, $CaTiO_3$ has a paraelectric phase. It has a dissipation factor (D) $\sim 10^{-3}$ and a dielectric permittivity above 180 at 1 KHz.[18] Accordingly this perovskite is classified as an incipient ferroelectric.[19] $CaTiO_3$ has been extensively studied due to its interesting structural and dielectric properties. These properties are modified by suitable substitutions in site A (Ca) or site B (Ti).[20–25] However, modification at the B-site has attracted surging attention owing to its important effect on the hybridization of the valence states between the O-ion and the B site ion. Among these ions, cobalt is found to be a good dopant which affects the electrical properties and show a continuous improvement in the structures of titanate and manganite perovskite.[26] However, a high dielectric loss ($\tan\delta$) is a huge obstacle in many applications. Nevertheless, the number of researches devoted to solving the large $\tan\delta$ problem is still very limited, and the results showed that this problem is very challenging.[27,28] Recently, doping barium titanate with cobalt has been proved to lower the temperature of the ferro–paraelectric phase transition

[a]*Laboratoire de la Matière Condensée et des Nanosciences, Département de Physique, Faculté des Sciences Université de Monastir, 5019, Tunisia. E-mail: crayssi@yahoo.com*

[b]*Laboratoire de Physique des Matériaux et des Nanomatériaux Appliquée à L'environnement, Faculté des Sciences de Gabes Cité Erriadh, 6079 Gabes, Tunisia*

Table 1 Experimental, calculated density and compactness of $Ca_{0.85}Er_{0.1}Ti_{(1-x)}Co_{4x/3}O_3$

Compounds	$x = 0$	$x = 0.05$	$x = 0.1$
Density (theo) (g cm^{-3})	4.350	4.404	4.460
Density (exp) (g cm^{-3})	4.263	4.271	4.280
Compactness: C	0.98	0.97	0.96

and increase the dielectric constant with a low dielectric loss.[29,30] These exciting results motivated us to dope cobalt in $CaTiO_3$ as higher dielectric constant materials can be used in capacitive components. In our work, the addition of a small amount of cobalt into $CaTiO_3$ leads to a decrease in its dielectric loss, which makes it suitable for microwave dielectric applications as resonators and filters[31] and it can also be used as a host for rare earth ions for efficient luminescence.[32] In the present paper, $Ca_{0.85}Er_{0.1}Ti_{1-x}Co_{4x/3}O_3$ ($CETCo_x$) (x = 0.00, 0.05 and 0.10), were prepared by sol–gel method. So, the purpose of the present work is to gain a deeper insight into the dielectric properties and their correlation with structural properties in the solid solution $CETCo_x$ by plotting the dielectric constant and loss as a function of frequency and temperature. The Curie–Weiss law and modified Curie–Weiss law allow us to better understand the dielectric phenomenon. The electrical modulus analysis is used to study the dielectric relaxation phenomenon and the electric process of the compounds.

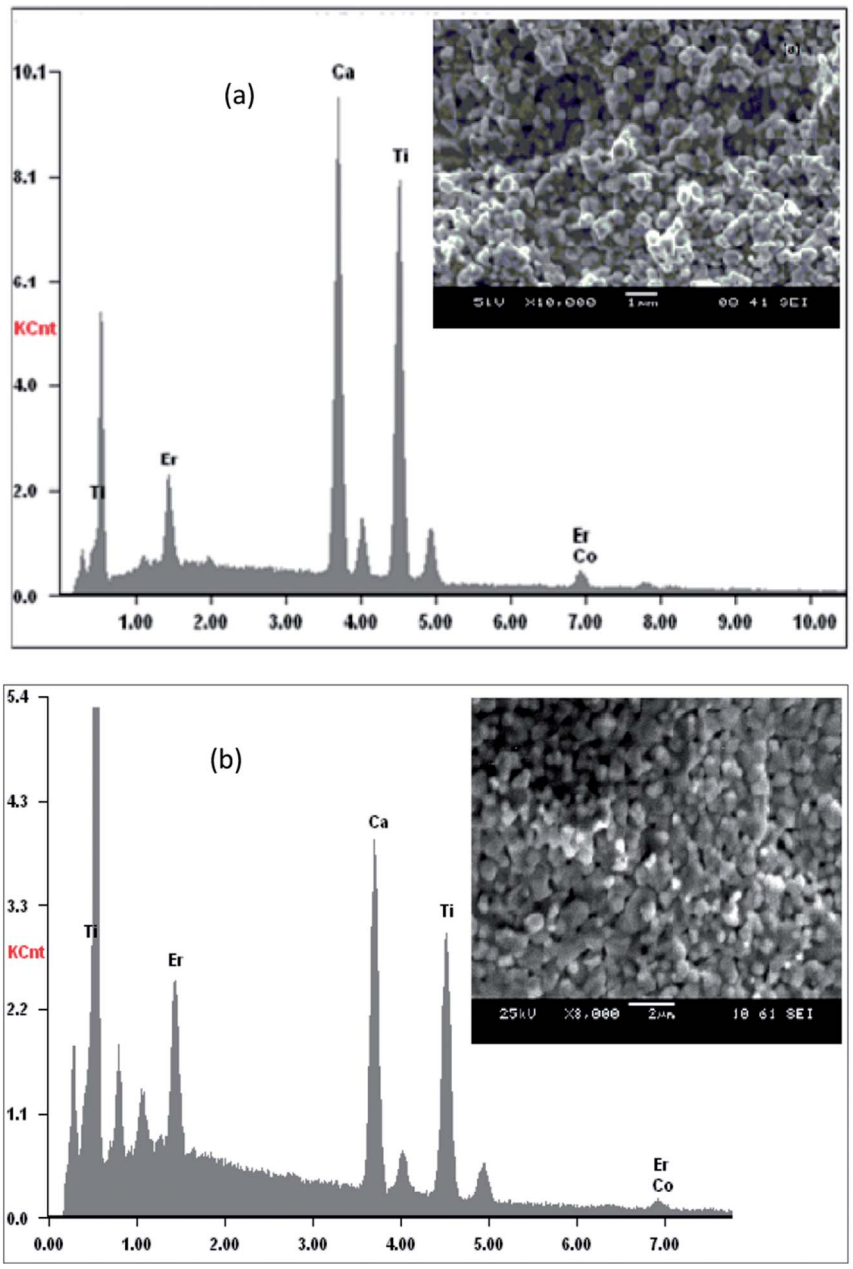

Fig. 1 (a and b): plot of EDX analysis of chemical species of $CETCo_x$ with (a) x = 0.00, and (b) x = 0.10. Inset shows their corresponding SEM graph.

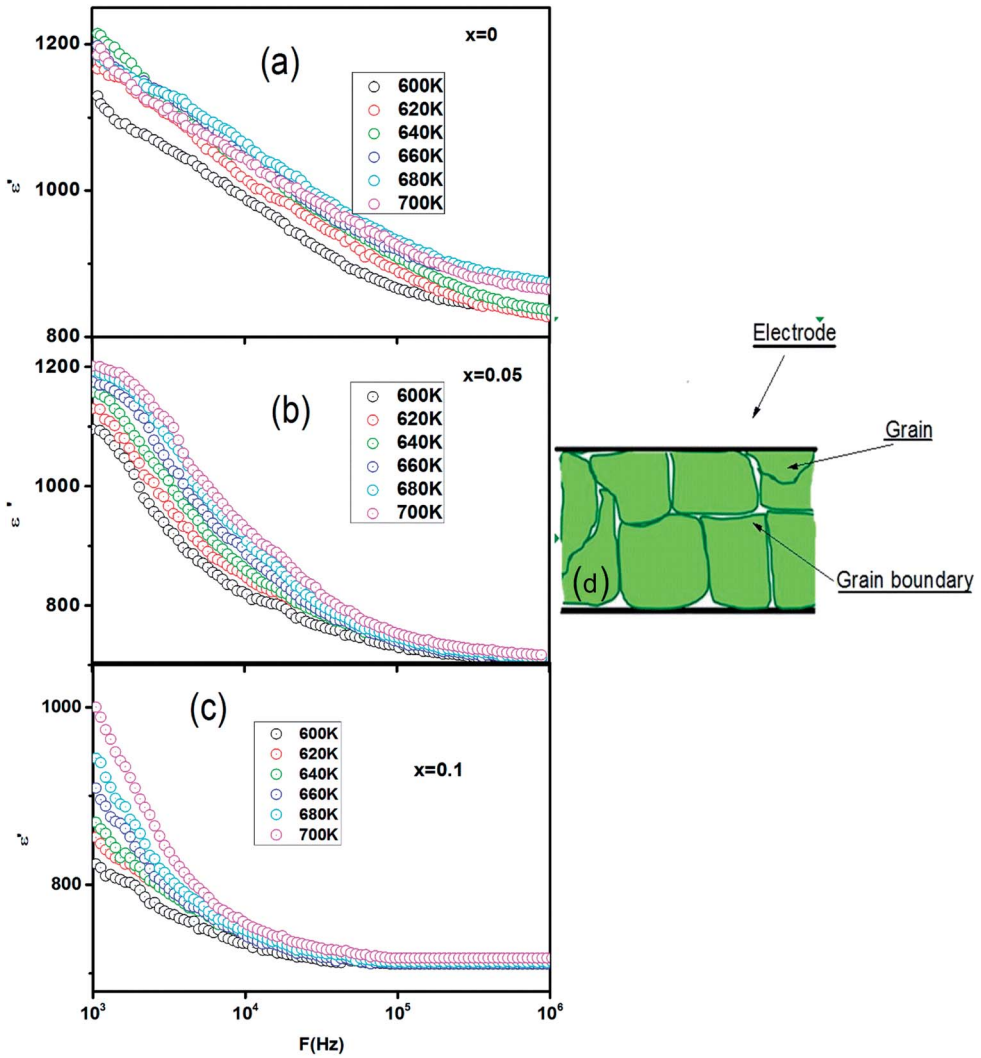

Fig. 2 (a–c): frequency dependence of real (ε') part of permittivity of $CETCo_x$ for $x = 0.00$, 0.05 and 0.10. (d): is a schematic structure of the samples.

2. Experimental procedure

Polycrystalline samples of the solid solution $CETCo_x$ ($x = 0.00$, 0.05 and 0.10) were prepared by sol–gel method. Highly pure powders of $CaCO_3$, TiO_2, Er_2O_3 and Co $Cl_2 \cdot 6H_2O$ were mixed in stoichiometric ratios. Details of the method of preparation and structure characterization were described in our previous work.[33] Phase purity, homogeneity, and crystallinity were identified by powder X-ray diffraction (XRD) analysis using an XPERT-PRO diffract-meter with a graphite monochromatized CuK_α radiation ($\lambda_{CuK\alpha} = 1.54$ Å). The data collected in the range of $0 \leq 2\theta \leq 100$ were analyzed by the FULLPROF software based on the Rietveld method. The XRD peaks was sharp and had a high intensity, indicating that the prepared samples have a high crystalline nature with a single-phase formation. Using Rietveld refinement of the XRD data, we indexed all peaks on the basis of an orthorhombic structure, with a *Pbnm* space group. The experimental density was calculated from the weight and geometrical dimensions of the cylindrical pellets and compared to the theoretical density $\rho_{theo} = ZM/N_AV$ where Z is the number of atoms in orthorhombic structure ($Z = 4$), M is the molecular weight $N_A = 6.02 \times 10^{23}$ mol^{-1} is Avogadro's number, and V is the volume of orthorhombic unit cell determined from X-ray measurements. The compactness was deduced from the ration $C = \rho_{exp}/\rho_{theo}$. Table 1 shows the values of ρ_{theo}, ρ_{exp} and C.

The dielectric measurements were performed on ceramic disks (pellets having a diameter of 8 mm and a thickness of 2 mm) after sputtering aluminum electrodes on their circular faces. After this step, an Agilent 4294A impedance analyzer and a cold plate of a liquid nitrogen cooled cryostat were used to collect capacitance C and conductance G measurements over a wide range of temperatures and frequencies.

3. Results and discussion

3.1 Morphological study

Fig. 1(a and b) shows the EDX spectra of pure and doped $CaErTiO_3$ (for $x = 0$ and 0.1) respectively. EDX spectra revealed the presence of Ca, Er, Ti, Co and O elements, which confirms

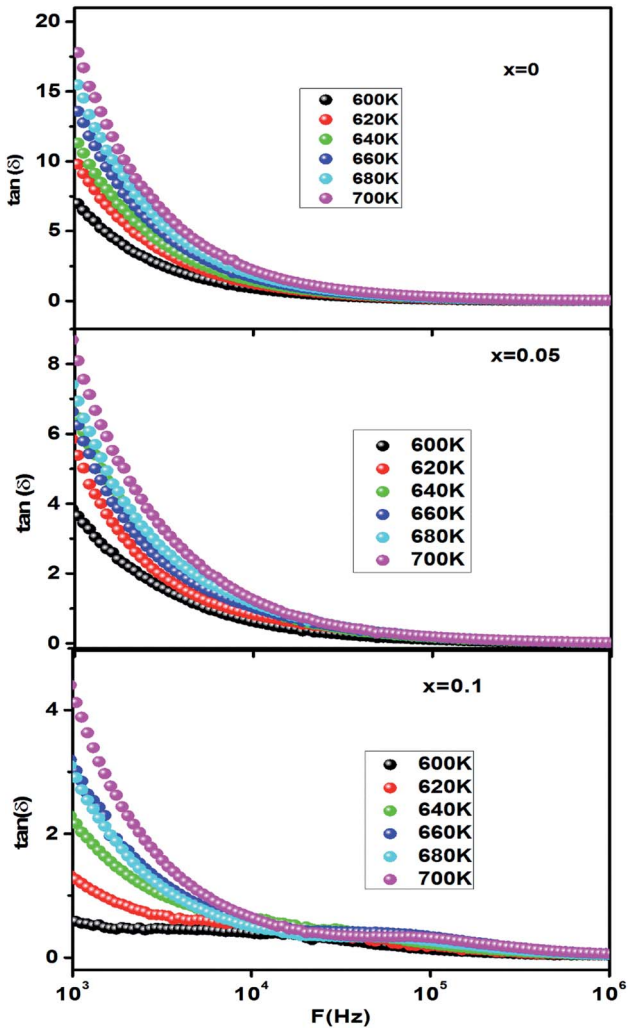

Fig. 3 Frequency dependence of dielectric loss of $CETCo_x$ for x = 0.00, 0.05 and 0.10.

that there is no loss of any integrated element during sintering, within the experimental errors. A typical microstructure of $CETCo_x$ (x = 0.00 and 0.10) is shown in the inset of Fig. 1(a and b) the micrograph indicated that the grains are uniformly distributed over the entire surface of the sample. It is interesting that the grain morphologies were consistent with the crystal structures.[34]

3.2 Dielectric study

3.2.1 Frequency dependence. The dielectric spectroscopic study provides insights into the structure of compounds, grain boundary, grain, transport properties and charge storage capabilities of dielectric material. The dielectric properties depend on several factors, including the chemical composition and the method of preparation, *etc.*[35,36]

The frequency dependence of the real part (ε') of permittivity of $CETCo_x$ (x = 0.00, 0.05 and 0.10) at different temperatures is shown in Fig. 2(a–c). The dielectric constant (ε') decreased rapidly with the increase in frequency. This decrease is due to

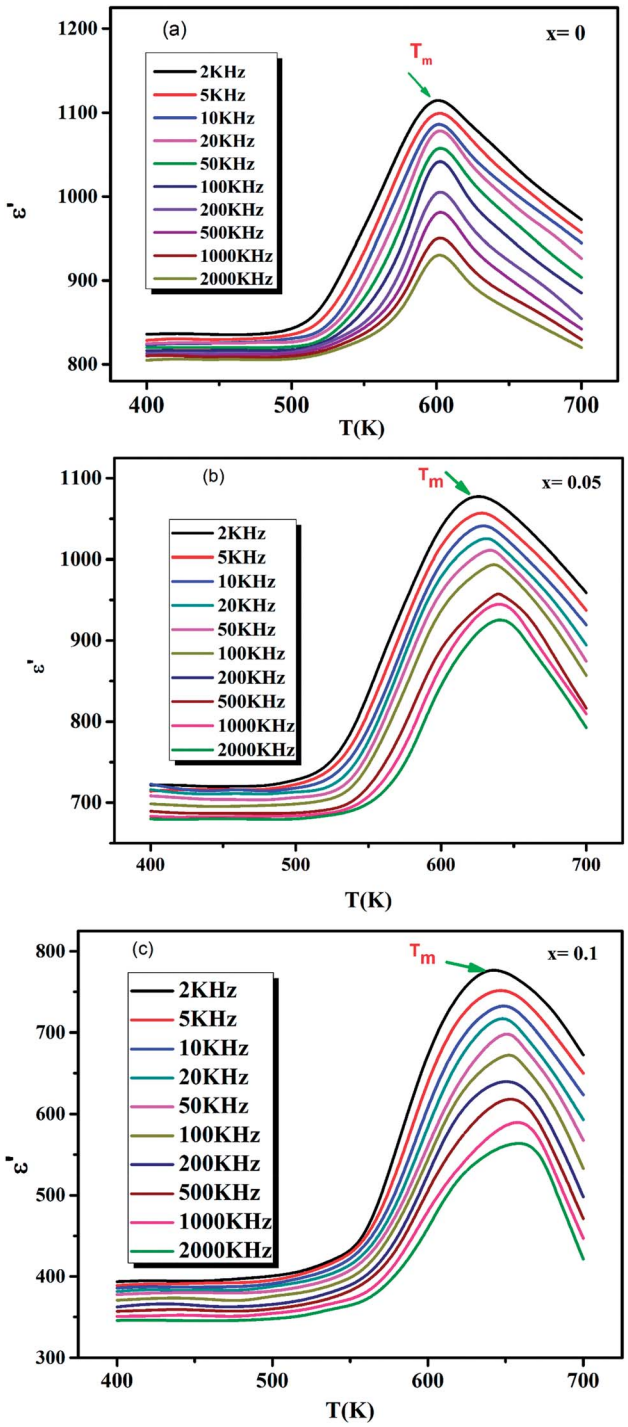

Fig. 4 (a–c) Temperature dependence of dielectric constant (ε') of $CETCo_x$ at different frequencies respectively for x = 0.00, 0.05 and 0.10.

the reduction of space charge polarization effect. Then, it remained nearly constant but, increased with increasing temperature at a given frequency. However, at low frequency the dielectric constant was high. This is due to the presence of space charge polarization at the grain boundaries, which generates a potential barrier. Then, an accumulation of charge at the grain boundary occurred, which led to higher values of

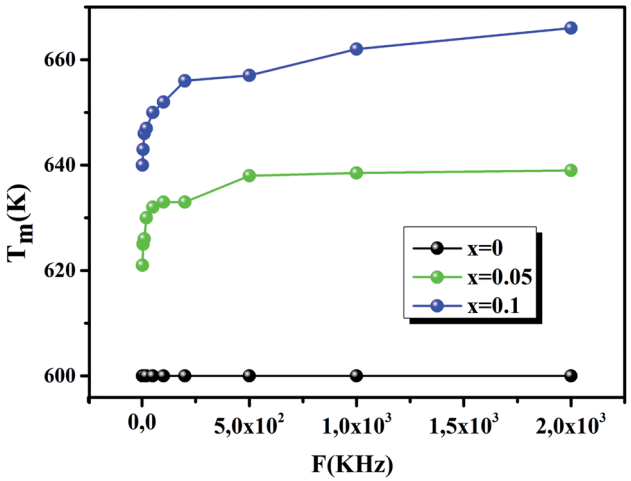

Fig. 5 The variation of T_m as a function of frequency for $x = 0.00$, 0.05 and 0.10.

the real part of permittivity.[37] The dielectric dispersion can be explained by the dominance of grain boundaries' effect rather than by the grains. This is attributed to Maxwell–Wagner type of interfacial polarization in accordance with Koop's phenomenological theory.[38,39]

The dielectric loss tangent, tan(δ), is related to the dielectric relaxation process and is given as the ratio of the imaginary part ε'' and the real part ε', *i.e.*, $\tan(\delta) = \varepsilon''/\varepsilon'$. The dielectric loss represents the energy loss and occurs when the polarization shifts behind the applied electric field caused by the grain boundaries.

In general, the dielectric loss of dielectric materials originates from three distinct factors: space charge migration (interfacial polarization contribution), direct current (DC) conduction, and movement of the molecular dipoles (dipole loss).[40]

To explain the decrease of the real part of permittivity at higher frequencies, we supposed that the dielectric structure is composed of low resistive grains separated by poor conducting thin grain boundaries (as illustrated in Fig. 2(d)). As a result of the applied electric field, we obtained a localized accumulation of charges, which led to the interfacial polarization.[41]

The frequency dependence of the dielectric loss tangent at different temperatures is shown in Fig. 3. The curve shows the same behavior of the dielectric constant (ε'). The high value of tan(δ) at a low frequency can be attributed to the high resistivity of grain boundaries which are more effective than the grains.

The ionic radius of Co^{3+} is the same as that of Ti^{4+}, but it is much smaller than that of Ca^{2+}. Co^{3+} ions are more likely to replace Ti^{4+} ions for their similar ionic size. Thus the Co^{2+} ions act as electron acceptors in $CaTiO_3$ lattice and occupy Ti^{4+} ionic site. The molecular formula of the Co-doped $CaTiO_3$ can be written as $CaCo_xTi_{1-x}O_3$. As a result of this, the $CaTiO_3$ crystal is distorted. All the above data indicate that Co-doping influences the variation of T_c. It also can be seen that ε_{max} decreases with the increase of Co concentration. Tzing *et al.*[42] proposed that ε_{max} strongly depends upon the size of the grains.

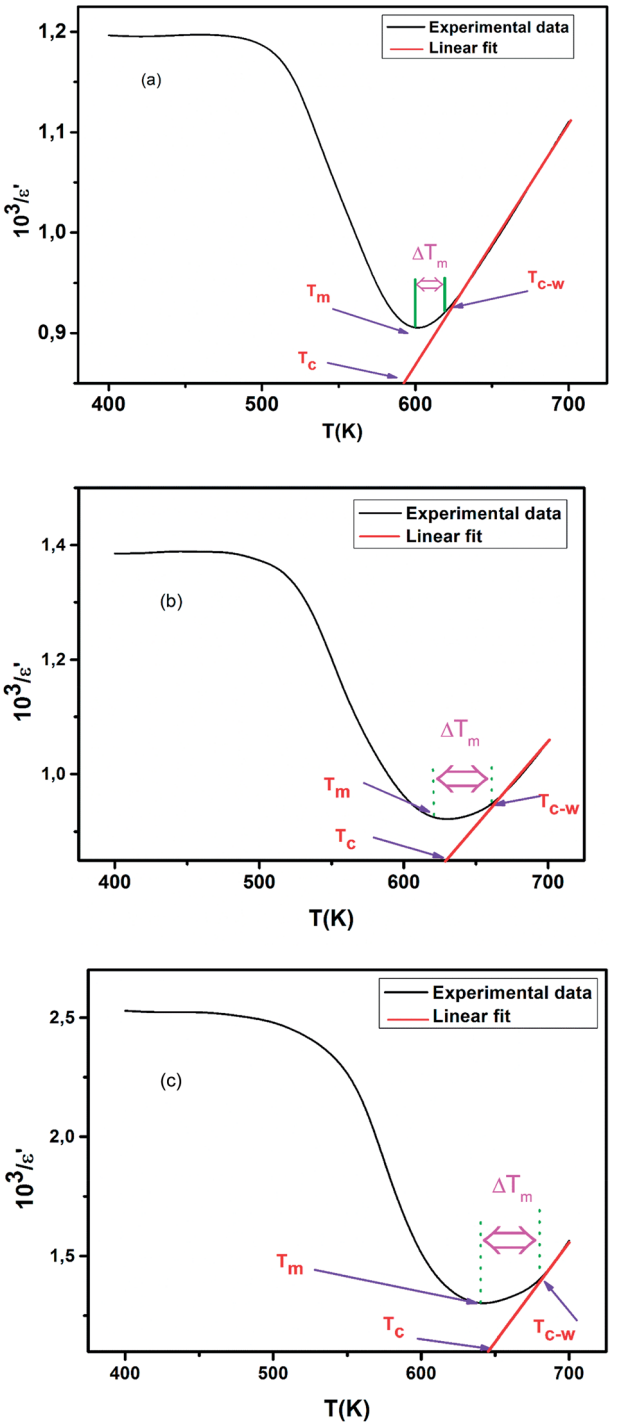

Fig. 6 (a–c): The inverse of dielectric constant ($10^3/\varepsilon'$) as a function of temperature at 2 kHz.

In fact, the dielectric constant of the materials is linearly proportional to the average value of grain size.[43] Therefore, the decrease of dielectric constant and loss tangent as a function of Co doping is due to the decrease of grain size, which is in agreement with the previous results (conduction mechanism).[33] This indicates that there is a strong relation between the conduction process and the dielectric polarization in these Co doped Ti. In addition, cobalt seems also to have an effect on the

Table 2 Parameters obtained from the temperature dependence of dielectric permittivity for 2 kHz

X	ε'_m (2 kHz)	T_m (K) (2 kHz)	ΔT_m (K) (2 kHz)	C (10^5 K) (2 kHz)	γ (2 kHz)
0.00	1114	600	25	6.75	1.04
0.05	1084	620	36	4.54	1.75
0.10	776	640	40	2.77	1.86

processing of $BaTiO_3$ ceramics since the grain boundary mobility decreases with Co doping due to the segregation, at the grain boundaries, of defects induced by doping.[44]

3.2.2 Temperature dependence. The variation of the real part (ε') of the dielectric permittivity as a function of temperature at various frequencies (2×10^3 to 2×10^6 Hz) of $CETCo_x$ with $0.00 \leq x \leq 0.10$ samples is carefully examined and shown in Fig. 4(a–c). It is observed that $\varepsilon'$is frequency and temperature independent at low temperature. Then, it increases gradually with increasing temperature to its maximum value (ε'_{max}) around 600 K, 620 K, 640 K for $x = 0.00$, 0.05 and 0.10, respectively, which corresponds to the transition from a ferroelectric to a paraelectric phase.[45] The study of the dielectric constant indicates that for $x = 0.00$ (Fig. 4(a)), the transition temperature value has no variation as a function of frequency, which confirms that these compositions are of classical ferroelectric type. Fig. 4(b and c) shows that the ferroelectric relaxor characteristic of a high frequency dispersion in the vicinity of T_c, a diffuse phase transition, a small shift towards high temperatures and a decrease in the value of the permittivity as function of frequency are accentuated as the concentration of Co^{3+} ions increased from $x = 0.05$ to 0.10.[46,47]

Fig. 5 shows the evolution of T_m as a function of frequency. It also shows that T_m is constant for pure $CaErTiO_3$, confirming the classical transition, but, it increases with increasing frequency for Co doped $CaErTiO_3$, confirming the relaxor behavior.

An inverse of relative permittivity ($10^3/\varepsilon'$) as a function of temperature at 2 kHz is plotted in Fig. 6(c–e) to explain the dielectric phenomenon in the solid solution $CETCo_x$ by Curie–Weiss law. This method describes the ferro–paraelectric transition in the region and is expressed by the following relation:

$$\frac{1}{\varepsilon'} = \frac{T - T_C}{C} \quad (1)$$

where C is the Curie–Weiss constant and T_c is the Curie–Weiss temperature.

To show the degree of deviation from the relation (1), we define the parameter ΔT_m by the following expression:[48]

$$\Delta T_m = T_{C-W} - T_m \quad (2)$$

Where T_m denotes the temperature of the dielectric constant maximum (ε'_{max}) and T_{C-W} represents the temperature from which the dielectric constant starts to deviate from the Curie–Weiss law.

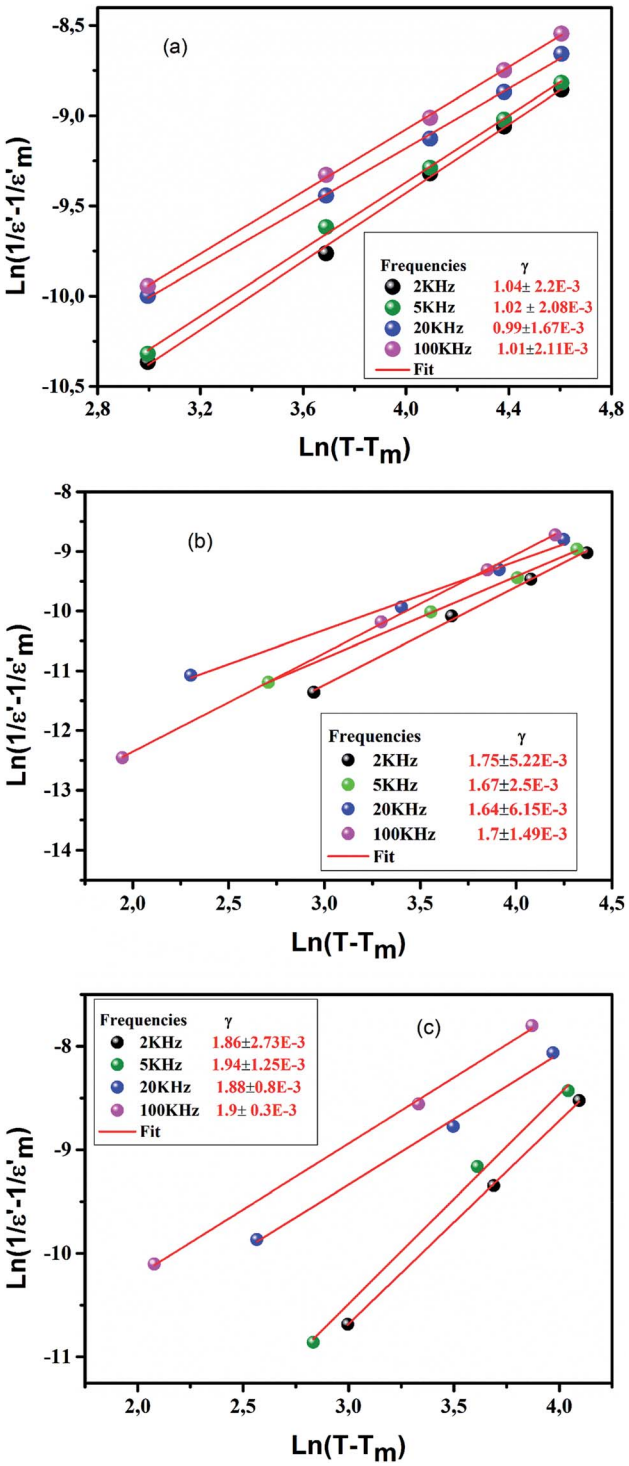

Fig. 7 (a–c): the plot of $\ln(1/\varepsilon - 1/\varepsilon'_{max})$ as a function of $\ln(T - T_m)$ at 2, 5, 20 and 100 kHz for $Ca_{0.85}Er_{0.1}Ti_{1-x}Co_{4x/3}O_3$.

Above T_c, the linear fit is examined in the paraelectric region. The fitting parameters, *i.e.* the Curie–Weiss constant (C) and the Curie temperature T_c are listed in Table 2 at 2 kHz.

Note that the Curie–Weiss law was used to determine the degree of disorder in the solid solutions using an empirical

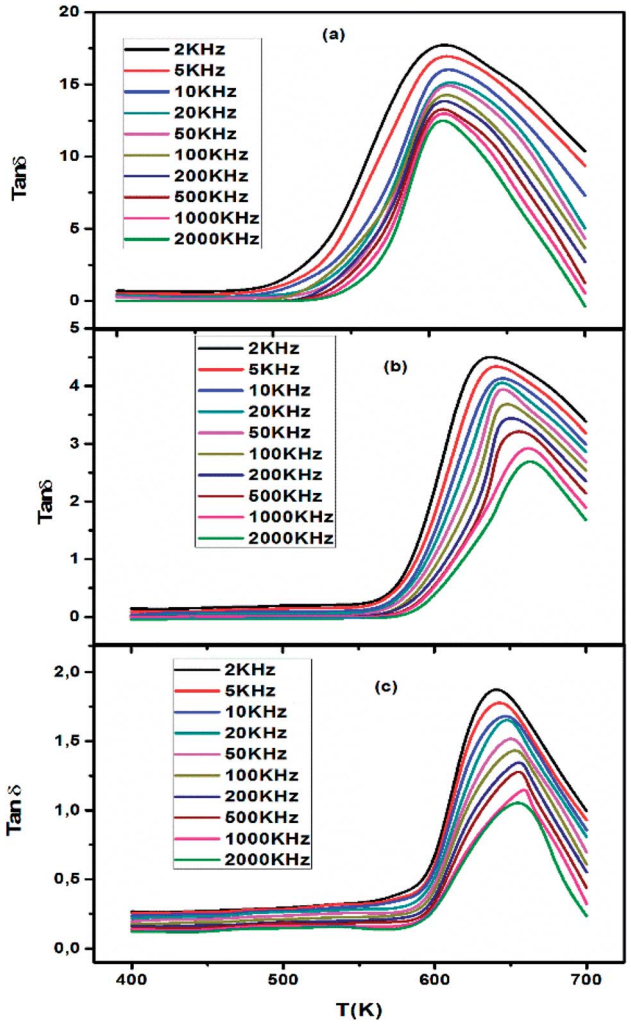

Fig. 8 Temperature dependence of dielectric loss (tan δ) of CETCo$_x$ at different frequencies.

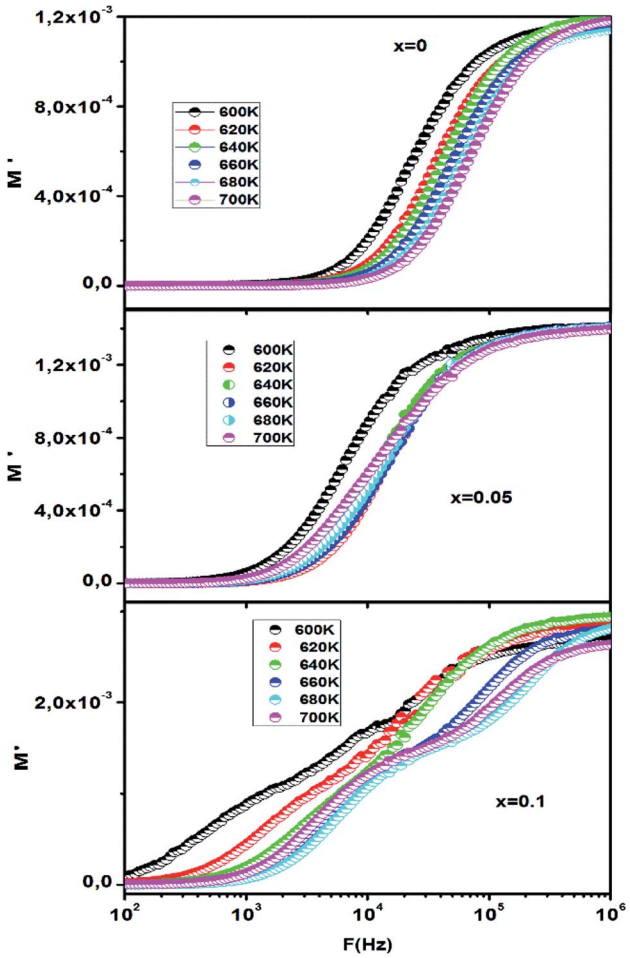

Fig. 9 Frequency dependencies of M' at different temperatures respectively for $x = 0.00$, 0.05 and 0.10.

formula developed by Uchino *et al.* for $T > T_m$. This leads us to use the modified Curie–Weiss law as given below:[49]

$$\frac{1}{\varepsilon'} - \frac{1}{\varepsilon'_{max}} = \frac{(T - T_m)^\gamma}{C} \quad (3)$$

γ is the diffuseness coefficient which shows the character of the phase transition.[50] For $\gamma = 1$, a classical transition in which Curie–Weiss law is obeyed, for $1 < \gamma < 2$ is a diffuse transition and for $\gamma = 2$ is an ideal relaxor ferroelectric.[51] The plots of $\ln\left(\frac{1}{\varepsilon'} - \frac{1}{\varepsilon'_{max}}\right)$ *versus* $\ln(T - T_m)$ for CETCo$_x$ at frequencies of 2, 5, 20 and 100 kHz are displayed in Fig. 7(a–c). The same behavior is observed for the other frequencies. The γ of these frequencies for different concentration of Co are presented in Fig. 7(a–c). From this figure, we note that diffuseness coefficient γ is found to be around 1 for $x = 0$ which indicate a classical transition. However, γ value is between 1 and 2 ($1 < \gamma < 2$) for doped $CaErTiO_3$, indicating a diffuse behavior. However, the obtained value of γ present an independent behavior with the effect of frequency.

Fig. 8(a–c) shows the dielectric loss (tan δ) as a function of temperature at various frequencies. The variation of tan δ with frequency shows a similar nature as the variation of ε' with frequency. It is seen from the figure that the dielectric loss initially decreases rapidly with increasing frequency, exhibiting a dispersion at lower frequencies, and then remains fairly constant at higher frequencies. However, with the increase in the frequency of the applied field the mechanisms of polarization such as space charge, orientation, and ions start lagging behind the field and, thus, dielectric loss decreases. Meanwhile, the variation of the dielectric loss with temperature exhibits the same nature as that of the variation of dielectric constant with temperature and could be explained in the same way as that used for discussing the dielectric constant. It is found that with the increase in temperature, the dielectric loss increases. The mobility of charge carriers increases with temperature which increases the polarization and leads to high dielectric loss. The observed higher value of dielectric loss at high temperature is due to charge accumulation at grain boundaries.[47]

3.3 Electrical modulus analysis

The electrical response can be analyzed by the complex electric modulus [$M^*(\omega)$] formalism. It is used to investigate the

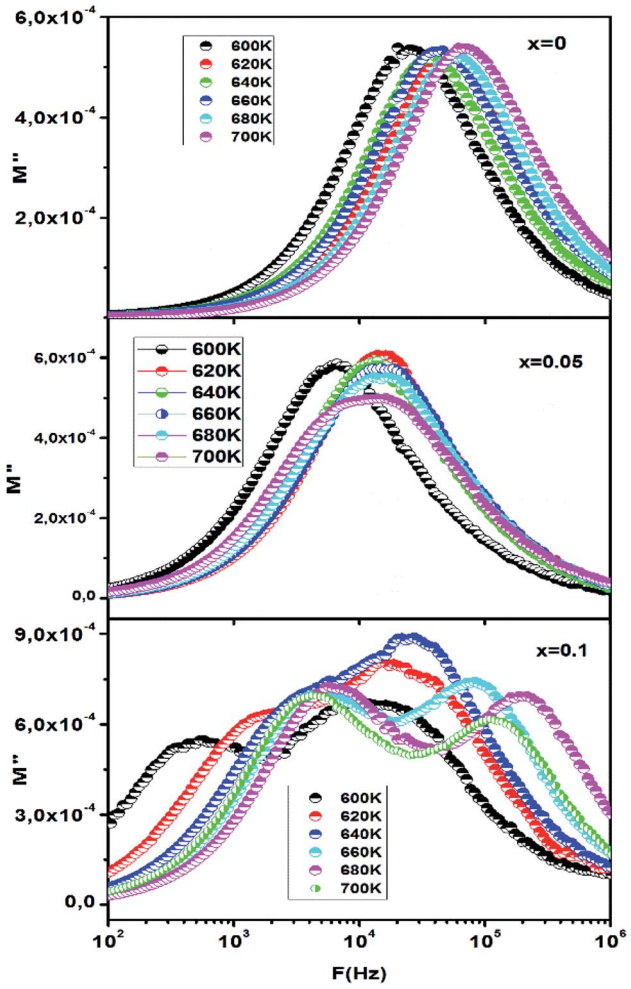

Fig. 10 Frequency dependencies of M'' at different temperatures respectively for $x = 0.00$, 0.05 and 0.10.

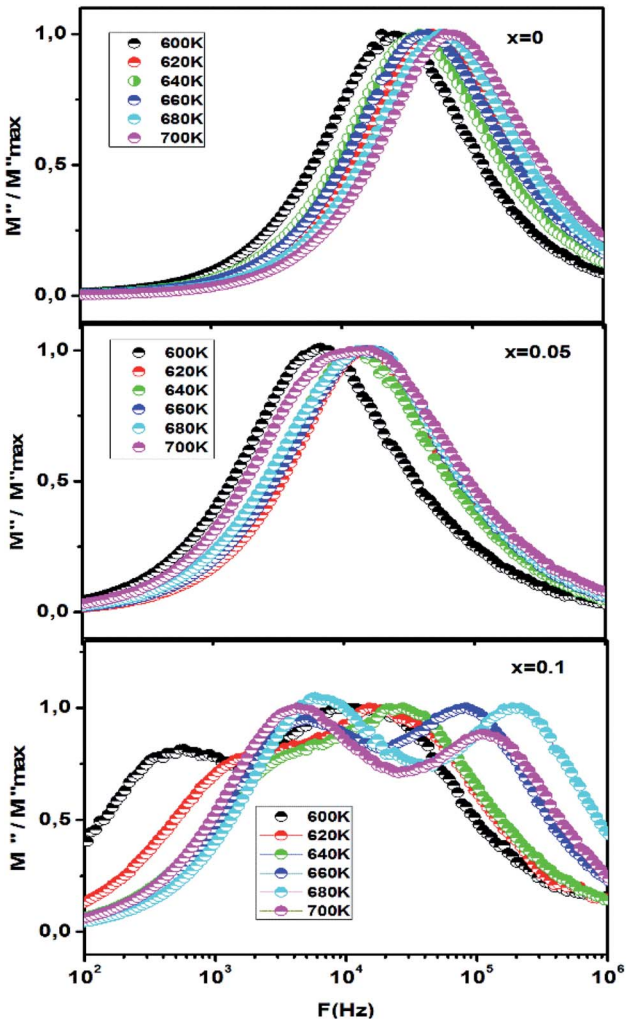

Fig. 11 The normalized imaginary part of modulus M''/M''_{max} *vs.* frequency plot, of $CETCo_x$ for $x = 0.00$, 0.05 and 0.10.

dielectric relaxation processes of the compounds. The complex electric modulus was calculated from the dielectric permittivity $[\varepsilon^*(\omega)]$ using the following relation.[52–55]

$$M^*(\omega) = \frac{1}{\varepsilon^*} = \frac{1}{\varepsilon' - j\varepsilon''} = \frac{\varepsilon'}{\varepsilon'^2 - \varepsilon''^2} + j\frac{\varepsilon''}{\varepsilon'^2 - \varepsilon''^2} = M' + jM'' \quad (4)$$

where $M' = \frac{\varepsilon'}{\varepsilon'^2 - \varepsilon''^2}$ and $M'' = \frac{\varepsilon''}{\varepsilon'^2 - \varepsilon''^2}$: (M', ε') and (M'', ε'') are the real and imaginary components of modulus and permittivity, respectively, and $j = \sqrt{-1}$ is the imaginary factor.

The physical significance of the electrical modulus is the relaxation mechanism of the electric field in the material when the electric displacement remains constant. The frequency dependent characteristics of the real (M') and imaginary (M'') parts of the electrical modulus are excellent methods to investigate the relaxation process.[56]

The frequency dependence of the real part (M') of $CETCo_x$ at different temperatures is shown in Fig. 9. At low frequency, the M' value is found to be nearly zero and increases when increasing frequency. This continuous dispersion on increasing frequency can be attributed to the conduction process due to the short range mobility of charge carriers. It can also be related to the absence of the restorative force which governs the mobility of charge carriers under the action of an induced electric field.[57–59] A saturation value (the plateau region) is reached at high frequency, suggesting that the electrical properties of the materials are frequency-independent. Moreover, this feature indicates the negligible contribution of electrode polarization in the synthesis of $CETCo_x$.[60]

We can deduce from Fig. 9 ($x = 0.1$) that M' exhibits three plateau regions, which indicates the existence of three different relaxation dynamics.[61] These three plateau regions existing in M' of the modulus are correlated with the imaginary part M'', as shown in Fig. 8 ($x = 0.1$).

The evolution of the imaginary part (M'') of the modulus as a function of frequency at different temperatures is shown in Fig. 10. The imaginary part of the modulus (M'') exhibits a single relaxation peak ($x = 0.00$, $x = 0.05$), centered at the dispersion region of the real part of the modulus (M') associated with the grain effect. For $x = 0.10$, it displays a flat peak response, but it is in fact a double peak response Fig. 10 ($x = 0.1$). The corresponding relaxation of M'' peaks shifted to the higher frequency

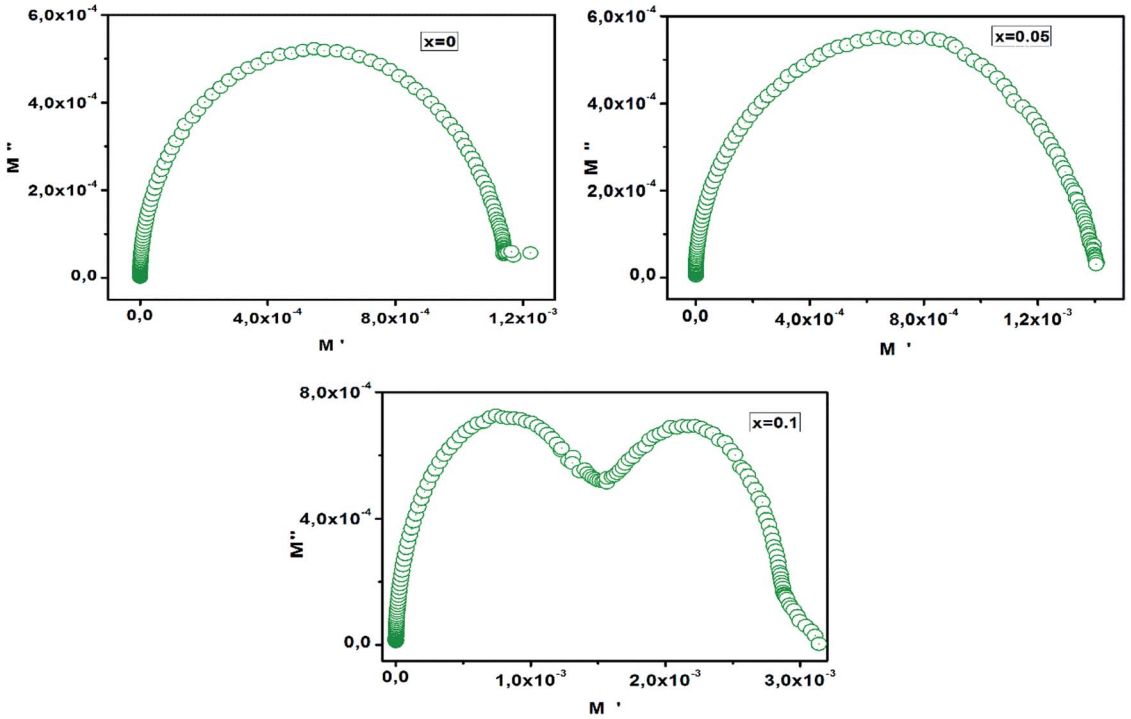

Fig. 12 Cole–Cole (M'' *vs.* M') plot.

when increasing temperature and the charge carriers movement becomes faster, resulting in a decrease in relaxation time.[18,62] This behavior confirms that the relaxation is temperature dependent, and that the charge carriers hopping is taking place.[57,63] The plot of the imaginary part of the electric modulus (M'') represents two parts. The first part, at low frequency *i.e.* the region on the left of the peak presents the frequencies range in which the ions can move over long distance *i.e.* ions can successfully jump from one site to the neighboring site. The second part, at high frequency *i.e.* the frequency above maximum (the region on the right of the peak) shows the region in which ions are confined to their potential wells.[64]

The variation in the peak position of the real part and the imaginary part of the modulus of $CETCo_x$ is related to the variation in the microstructure and cation distribution with temperature. Furthermore, the asymmetric broadening of the imaginary part peaks suggests that the conduction mechanism is related to non-Debye type.[65]

The normalized imaginary part of the modulus M''/M''_{max} as a function of frequency at different temperatures is shown in Fig. 11. The normalized functions of M''/M''_{max} is used to prove that the relaxation mechanism is dominated by the long-range or the short-range movement of charge carriers.[66] We can notice from Fig. 11 that the separation between the normalized M'' peaks indicates that the relaxation mechanism is dominated by the short range movement of charge carriers. In addition, the broadening of the observed peaks indicates the existence of electrical mechanism with a spread of the time relaxation processes.[67]

The Cole–Cole plot (M'' *vs.* M') for $CETCo_x$ (x = 0.00, 0.05, 0.10) at T = 680 K is shown in Fig. 12. The Cole–Cole plot (M'' *vs.* M') is more effective than the Nyquist plot of impedance (Z'' *vs.* Z') in separating the relaxation effects from grains (conducting regions) and grain boundaries (resistive plates) in materials. We can notice from Fig. 12 the existence of one semicircle for x = 0.00 and 0.05, indicating that the grain boundaries effect is

Table 3 The calculated values boundary (τ) relaxation time of $CETCo_x$ at different temperature for all compounds

	$x = 0.00$			$x = 0.05$			$x = 0.10$		
T (K)	M''_{max} (10^{-4})	f_{max} (Hz)	τ (s) (10^{-5})	M''_{max} (10^{-4})	f_{max} (Hz)	τ (s) (10^{-5})	M''_{max} (10^{-4})	f_{max} (Hz)	τ (s) (10^{-5})
600	5.3876	20 260	78, 556	5.7917	7727	2, 0597	6.711	9652	1, 6489
620	5.2041	39 480	40, 312	6.0695	12 980	1, 2261	8.0635	15 060	1, 0568
640	5.2273	45 790	34, 757	5.9102	13 980	1, 1384	8.8870	27 250	0, 584
660	5.3369	49 310	32, 276	5.7489	13 980	1, 1384	7.4190	82 850	0, 1921
680	5.2223	57 190	27, 829	5.5156	15 060	1, 0568	6.9366	111 500	0, 1873
700	5.3866	61 590	25, 841	4.9890	16 220	0, 9812	6.1743	187 300	0, 0849

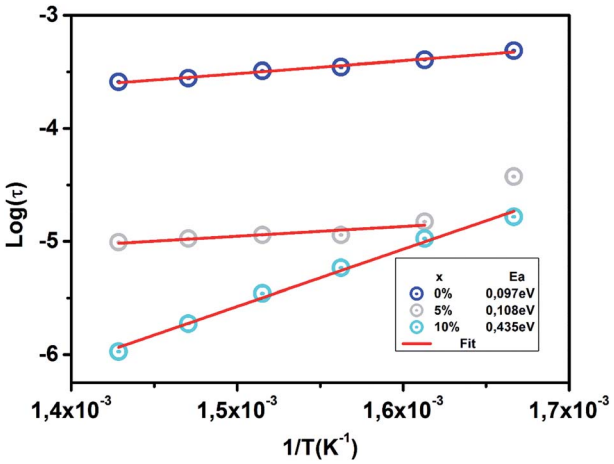

Fig. 13 Variation of relaxation time (τ) with inverse temperature ($1/T$) of $CETCo_x$ for $x = 0.00$, 0.05 and 0.10.

more dominant than the grain effect in the conduction mechanism.[68,69] For $x = 0.10$ the Cole–Cole plot shows the existence of two successive semi-circular peaks. The first semicircle is attributed to the contribution of grain boundary (interfacial properties) and the second one is associated to the grain (bulk properties). This indicates the existence of two relaxation processes with two relaxation times (τ) for each relaxation.

The relaxation time (τ) is determined from the peak height of the plot of M'' *versus* frequency (Fig. 10), which reveals the short range or the long range movement of charge carriers.[70] It can be calculated using the following expression:

$$\tau_{gb} = \frac{1}{2\Pi f_{max}},$$

where f_{max} is the relaxation frequency.

The calculated value of the relaxation time is presented in Table 3.

The evolution of the relaxation time of grain boundary as a function of $1/T$ is shown in Fig. 13.

The activation energy in the relaxation mechanism is determined by the temperature-dependent τ_{gb}, which obeys the Arrhenius law based on the following relation:

$$\tau_{gb} = \tau_0 \exp\left(\frac{E_a}{KT}\right)$$

where τ_0 is the pre-exponential factor, E_a is the activation energy, k is Boltzmann constant, and T is the absolute temperature.

The grain boundary activation energy value is calculated from the slope of $\mathrm{Log}(\tau_{gb})$ *versus* $1/T$ and mentioned in Fig. 13. The activation energy value suggests that the high-temperature dielectric relaxation is also a thermally-activated process.[71] The E_a value increases with the increase of Co rate. This result can be associated with the lower value of conductivity which supports the resistive nature of doped sample. However, for higher values of x, the grain boundary thickness with high resistance increases; therefore, more energy is required for the hopping of electrons between ions.

4. Conclusion

$CETCo_x$ samples were successfully synthesized by sol–gel method. The dielectric properties of $CETCo_x$ were investigated. The dielectric permittivity (ε') plot as a function of temperature shows a classic phenomenon for $x = 0.00$. Then, a small shift was observed for $x = 0.05$ and 0.10, which proves the existence of a relaxor phenomenon. The plot of the dielectric constant presents a maximum (ε'_{max}) at high temperature explained by the space charge polarization. This fact is caused by the imperfection in materials and the mobility of ions. Results, also, show that the dielectric loss ($\tan\delta$) as a function of temperature has the same evolution of ε'. This observation confirms the relaxor process. In order to explain the dielectric phenomenon, we used the Curie–Weiss law and modified Curie–Weiss law. The electrical properties of our compounds deduced from the complex electric modulus show a conduction process due to the short range mobility of charge carriers. The imaginary part of the modulus proves that the relaxation is temperature dependent, and that the charge carriers' hopping is taking place.

Conflicts of interest

There are no conflicts to declare.

References

1 T. Xu, L. Chen, Z. Guo and T. Ma, Strategic improvement of the long-term stability of perovskite materials and perovskite solar cells, *Phys. Chem. Chem. Phys.*, 2016, **18**, 27026–27050.
2 B. Luo, X. Wang, E. Tian, G. Li and L. Li, Electronic structure, optical and dielectric properties of $BaTiO_3/CaTiO_3/SrTiO_3$ ferroelectric superlattices from first-principles calculations, *J. Mater. Chem. C*, 2015, **3**, 8625–8633.
3 J. F. Scott, Applications of Modern Ferroelectrics, *Science*, 2007, **315**, 954–959.
4 X. Na Zhu, X. Chen, H. Tian and X. M. Chen, Atomic scale investigation of enhanced ferroelectricity in (Ba, Ca) TiO_3, *RSC Adv.*, 2017, **7**, 22587–22591.
5 K. Uchino, Relaxor ferroelectric devices, *Ferroelectrics*, 1994, **151**, 321–330.
6 V. Westphal, W. Kleemann and M. D. Glinchuk, Diffuse Phase Transitions and Random-Field-Induced Domain States of the "Relaxor" Ferroelectric $PbMg_1/3Nb_2/3O_3$, *Phys. Rev. Lett.*, 1992, **68**, 847–850.
7 A. E. Souza, S. R. Teixeira, C. M. -Santos, W. H. Schreiner, P. N. Lisboa Filhod and E. Longo, Photoluminescence activity of $Ba_{1-x}Ca_xTiO_3$: dependence on particle size and morphology, *J. Mater. Chem. C*, 2014, **2**, 7056–7070.
8 H. Zheng, H. Bagshaw, G. D. C. C. Györgyfalva, I. M. Reaney, R. Ubic and J. Yerwood, Raman spectroscopy of B-site order–disorder in $CaTiO_3$-based microwave ceramics, *J. Eur. Ceram. Soc.*, 2003, 2653–2659.
9 B. G. Kim, S. M. Cho, T. Y. Kim and H. M. Jang, Giant Dielectric Permittivity Observed in Pb-Based Perovskite Ferroelectrics, *Phys. Rev. Lett.*, 2001, **86**, 3404–3406.

10 J. B. Wu, C. W. Nan, Y. H. Lin and Y. Deng, Giant Dielectric Permittivity Observed in Li and Ti Doped NiO, *Phys. Rev. Lett.*, 2002, **89**, 217601–217604.

11 W. Dong, B. Li, X. Wang, L. An, C. Li, B. Chen, G. Wang and Z. Shi, General Approach to Well-Defined Perovskite $MTiO_3$ (M = Ba, Sr, Ca, and Mg) Nanostructures, *J. Phys. Chem. C*, 2011, **115**, 3918–3925.

12 S. Lazaro, J. Milanez, A. T. Figueiredo, V. Longo, V. R. Mastelaro, F. S. Vicente, A. C. Hernandes, J. A. Varela and E. Longo, Relation between photoluminescence emission and local order-disorder in the $CaTiO_3$ lattice modifier, *Appl. Phys. Lett.*, 2007, **90**, 111904–111906.

13 V. S. Marques, L. S. Cavalcante, J. C. Sczancoski, D. P. Volanti, J. W. M. Espinosa, M. R. Joya, M. R. M. C. Santos, P. S. Pizani, J. A. Varela and E. Longo, Influence of microwave energy on structural and photoluminescent behavior of $CaTiO_3$ powders, *Solid State Sci.*, 2008, **10**, 1056–1061.

14 A. P. Rodrigues, M. Inoue, T. Tanaka, M. Miyake, A. M. Sfer, E. Kishimoto, H. Tsujigiwa, R. S. Rivera and H. Nagatsuka, Effect of $CaTiO_3$–$CaCO_3$ prepared by alkoxide method on cell response, *J. Biomed. Mater. Res., Part A*, 2009, **93**, 297–303.

15 L. Sun, R. Zhangb, Z. Wangb, E. Caob, Y. Zhangb and L. Juc, Microstructure, dielectric properties and impedance spectroscopy of Ni doped $CaCu_3Ti_4O_{12}$ ceramics, *RSC Adv.*, 2016, **6**, 55984–55989.

16 B. Jancar, D. Suvorov, M. Valant and G. Drazic, Characterization of $CaTiO_3$-$NdAlO_3$ dielectric ceramics, *J. Eur. Ceram. Soc.*, 2003, **23**, 1391–1400.

17 G. Murugesan, R. Nithya, S. Kalainathan and Shamima Hussain, High temperature dielectric relaxation anomalies in $Ca_{0.9}Nd_{0.1}Ti_{0.9}Al_{0.1}O_{3-\delta}$single crystals, *RSC Adv.*, 2015, **5**, 78414–78421.

18 S. Sasaki, C. T. Prewitt and J. D. Bass, Orthorhombic perovskite $CaTiO_3$ and $CdTiO_3$: structure and space group, *Acta Crystallogr., Sect. C: Cryst. Struct. Commun.*, 1987, **43**, 1668–1674.

19 V. V. Lemanov, A. V. Sotnikov, E. P. Smirnova, M. Weihnacht and R. Kunze, Perovskite $CaTiO_3$ as an incipient ferroelectric, *Solid State Commun.*, 1999, **110**, 611–614.

20 H. S. Tewari, O. Parkash, V. B. Tare and D. Kumar, Dielectric properties of the system $Ca_{1-x}Y_xTi_{1-x}Co_xO_3$($0.00 \leq x \leq 0.15$), *J. Mater. Sci.*, 1990, **25**, 2181–2184.

21 C. Durga, P. H. S. Tewari, D. Kumar and O. Parkash, Dielectric properties of the system $Ca_{1-x}La_xTi_{1-x}Co_xO_3$, *Bull. Mater. Sci.*, 1988, **11**, 307–313.

22 D. Li and M. A. Subramanian, Noval tunable ferroelectric compositions: $Ba_{1-x}Ln_xTi_{1-x}M_xO_3$ (Ln=La, Sm, Gd, Dy. M=Al, Fe, Cr), *Solid State Sci.*, 2000, **2**, 507–512.

23 V. Vashook, L. Vasylechko, H. Ulmann and U. Guth, Synthesis, crystal structure, oxygen stoichiometry, and electrical conductivity of $La_{1-a}Ca_aCr_{0.2}Ti_{0.8}O_{3-\delta}$, *Solid State Ionics*, 2003, **158**, 317–325.

24 A. B. Hassen, F. I. H. Rhouma, J. Dhahri and N. Abdelmoula, Effect of the substitution of titanium by chrome on the structural, dielectric and optical properties in $Ca_{0.67}La_{0.22}Ti_{(1-x)}Cr_xO_3$ perovskites, *J. Alloys Compd.*, 2016, **663**, 436–443.

25 A. Hassini, M. Gervais, J. Coulon, V. T. Phuoc and F. Gervais, Synthesis of $Ca_{0.25}Cu_{0.75}TiO_3$ and infrared characterization of role played by copper, *Mater. Sci. Eng., B*, 2001, **87**, 164–168.

26 G. Mata Osoro, D. Bregiroux, M. Pham Thi and F. Levassort, *Mater. Lett.*, 2016, **166**, 259–262.

27 R. Mazumder, A. Seal, A. Sen and H. S. Maiti, *Ferroelectrics*, 2005, **326**, 103.

28 L. X. Feng, X. M. Tang, Y. Y. Yan, X. Z. Chen, Z. K. Jiao and G. H. Cao, *Phys. Status Solidi A*, 2006, **203**, 22.

29 Q. Li, J. Qi, Y. Wang, Z. Gui and L. Li, *J. Eur. Ceram. Soc.*, 2001, **21**, 2217–2220.

30 B. Cui, P. Yu, J. Tian and Z. Chang, *Mater. Sci. Eng., B*, 2006, **133**, 205–208.

31 B. Jancar, D. Suvorov, M. Valant and G. Drazic, *J. Eur. Ceram. Soc.*, 2003, **23**, 1391–1400.

32 K. Lemanski, A. Gagor, M. Kurnatowska, R. Pazik and P. J. Deren, *J. Solid State Chem.*, 2011, **184**, 2713–2718.

33 C. Rayssi, F. I. H. Rhouma, J. Dhahri, K. Khirouni, M. Zaidi and H. Belmabrouk, Structural, electric and dielectric properties of $Ca_{0.85}Er_{0.1}Ti_{1-x}Co_{4x/3}O_3$($0 \leq x \leq 0.1$), *Appl. Phys. A: Mater. Sci. Process.*, 2017, **123**, 778.

34 F. Bourguiba, A. Dhahri, T. Tahri, J. Dhahri, N. Abdelmoula, K. Taibi and E. K. Hlil, *J. Alloys Compd.*, 2016, **675**, 174–182.

35 A. Chandran and K. C. George, Defect induced modifications in the optical, dielectric, and transport properties of hydrothermally prepared ZnS nanoparticles and nanorods, *J. Nanopart. Res.*, 2014, **16**, 2238–2255.

36 M. D. Rahaman, M. D. Mia, M. N. I. Khan and A. K. M. Akther Hossain, Study the effect of sintering temperature on structural, microstructural and electromagnetic properties of 10% Ca-doped $Mn_{0.6}Zn_{0.4}Fe_2O_4$, *J. Magn. Magn. Mater.*, 2016, **404**, 238–249.

37 M. Abdullah Dar, K. Majid, K. Mujasam Batoo and R. K. Kotnala, Dielectric and impedance study of polycrystalline $Li_{0.35-0.5x}Cd_{0.3}Ni_xFe_{2.35-0.5x}O_4$ ferrites synthesized *via* a citrate-gel auto combustion method, *J. Alloys Compd.*, 2015, **632**, 307–320.

38 C. G. Koops, *Phys. Rev.*, 1951, **83**, 121.

39 L. Chauhan, A. K. Shukla and K. Sreenivas, Dielectric and magnetic properties of Nickel ferrite ceramics using crystalline powders derived from DL alanine fuel in sol–gel auto-combustion, *Ceram. Int.*, 2015, **41**, 8341–8351.

40 K. Yang, X. Huang, Y. Huang, L. Xie and P. Jiang, Fluoro-Polymer@$BaTiO_3$ Hybrid Nanoparticles Prepared *via* RAFT Polymerization: Toward Ferroelectric Polymer Nanocomposites with High Dielectric Constant and Low Dielectric Loss for Energy Storage Application, *Chem. Mater.*, 2013, **25**, 2327–2338.

41 H. Rahmouni, M. Smari, B. Cherif, E. Dhahri and K. Khirouni, *Dalton Trans.*, 2015, **44**, 10457–10466.

42 W. H. Tzing, W. H. Tuana and H. L. Lin, The effect of microstructure on the electrical properties of NiO-doped $BaTiO_3$, *Ceram. Int.*, 1999, **25**, 425–430.

43 P. Nayak, T. Badapanda, A. K. Singh and S. Panigrahi, *RSC Adv.*, 2017, **7**, 16319–16331.
44 M. N. Rahaman and R. J. Manalert, *J. Eur. Ceram. Soc.*, 1998, **18**, 1063–1071.
45 S. Yasmin, S. Choudhury, M. A. Hakim, A. H. Bhuiyan and M. J. Rahman, Structural and dielectric properties of pure and cerium doped barium titanate, *J. Ceram. Process. Res.*, 2011, **12**, 387–391.
46 F. Bahri and H. Khemakhem, Relaxor behavior and dielectric properties of $Ba_{1-x}Bi_{2x/3}Zr_{0.15}Ti_{0.85}O_3$ solid solution, *J. Alloys Compd.*, 2014, **593**, 202–206.
47 P. R. Das, L. Biswal, B. Behera and R. N. P. Choudhary, Structural and electrical properties of $Na_2Pb_2Eu_2W_2Ti_4X_4O_{30}$ (X = Nb, Ta) ferroelectric ceramics, *Mater. Res. Bull.*, 2009, **44**, 1214–1218.
48 J. Hao, W. Bai, W. Li and J. Zhai, Correlation Between the Microstructure and Electrical Properties in High-Performance $(Ba_{0.85}Ca_{0.15})(Zr_{0.1}Ti_{0.9})O_3$ Lead Free Piezoelectric Ceramics, *J. Am. Ceram. Soc.*, 2012, **95**, 1998–2006.
49 K. Uchino and S. Nomura, Critical exponents of the dielectric constants in diffused-phase-transition crystals, *Ferroelectr., Lett. Sect.*, 1982, **44**, 55–61.
50 A. Megriche, A. Mgaidi and C. Sarkis, Synthese Et Caracterisation De Ceramiques 0,75 Pb $(Mg_{1/3}Nb_{2/3})O_3$ – $0{,}25PbTiO_3$ Pures Et Dopees, *J. Soc. Alger. Chim.*, 2010, **20**, 27–34.
51 G. A. Smolenskii, Physical phenomena in ferroelectrics with diffused phase transition, *J. Phys. Soc. Jpn.*, 1970, **28**, 26.
52 P. B. Macedo, C. T. Moynihan and R. Bose, Role of ionic diffusion in polarization in vitreous ionic conductors, *Phys. Chem. Glasses*, 1972, **13**, 171.
53 M. Ganguly, M. Harish Bhat and K. J. Rao, Lithium ion transport in Li_2SO_4–Li_2O–B_2O_3 glasses, *Phys. Chem. Glasses*, 1999, **40**, 297–304.
54 S. Ghosh and A. Ghosh, Electrical conductivity and conductivity relaxation in mixed alkali fluoride glasses, *Solid State Ionics*, 2002, **149**, 67–72.
55 S. Lanfredi, P. S. Saia, R. Lebullenger and A. C. Hernandes, Electric conductivity and relaxation in fluoride, fluorophosphate and phosphate glasses: analysis by impedance spectroscopy, *Solid State Ionics*, 2002, **146**, 329–339.
56 M. Kaiser, Magnetic and electric modulus properties of In substituted Mg–Mn–Cu ferrites, *Mater. Res. Bull.*, 2016, **73**, 452–458.
57 R. Ranjan, R. Kumar, N. Kumar, B. Behera and R. N. P. Choudhary, Impedance and electric modulus analysis of Sm-modified $Pb(Zr_{0.55}Ti_{0.45})_{1-x/4}O_3$ ceramics, *J. Alloys Compd.*, 2011, **509**, 6388–6394.
58 M. Hanief Najar and K. Majid, Investigation of the transport properties of PPy/[Co (EDTA) NH 3 Cl] · H 2 O nanocomposite prepared by chemical oxidation method, *RSC Adv.*, 2016, **6**, 25449–25459.
59 J. Hazarika and A. Kumar, Electric modulus based relaxation dynamics and ac conductivity scaling of polypyrrole nanotubes, *Synth. Met.*, 2014, **198**, 239–247.
60 M. M. Costa, G. F. M. Pires Jr, A. J. Terezo, M. P. F. Grac and A. S. B. Sombra, Impedance and modulus studies of magnetic ceramic oxide $Ba_2Co_2Fe_{12}O_{22}$ (Co_2Y) doped with Bi_2O_3, *J. Appl. Phys.*, 2011, **110**, 034107.
61 C. Behera, P. R. Das and R. N. P. Choudhary, Structural and Electrical Properties of Mechanothermally Synthesized $NiFe_2O_4$ Nanoceramics, *J. Electron. Mater.*, 2014, **43**, 3539–3549.
62 Y. Ben Taher, N. Moutia, A. Oueslati and M. Gargouri, Electrical properties, conduction mechanism and modulus of diphosphate compounds, *RSC Adv.*, 2016, **6**, 39750–39757.
63 F. Borsa, D. R. Torgeson, S. W. Martin and H. K. Patel, Relaxation and fluctuations in glassy fast-ion conductors: Wide-frequency-range NMR and conductivity measurements, *Phys. Rev. B: Condens. Matter Mater. Phys.*, 1992, **46**, 795–800.
64 R. Schmidt, S. Pandey, P. Fiorenza and D. C. Sinclair, Non-stoichiometry in "$CaCu_3Ti_4O_{12}$" (CCTO) ceramics, *RSC Adv.*, 2013, **3**, 14580–14589.
65 A. Sinha and A. Dutta, Microstructure evolution, dielectric relaxation and scaling behavior of Dy-for-Fe substituted Ni-nanoferrites, *RSC Adv.*, 2015, **5**, 100330–100338.
66 A. Chen, Y. Zhi and L. E. Cross, Oxygen-vacancy-related low-frequency dielectric relaxation and electrical conduction in Bi: $SrTiO_3$, *Phys. Rev. B: Condens. Matter Mater. Phys.*, 2000, **62**, 228–236.
67 R. S. Yadav, I. Kuřitka, J. Vilcakova, P. Urbánek, M. Machovsky, M. Masař and M. Holek, Structural, magnetic, optical, dielectric, electrical and modulus spectroscopic characteristics of $ZnFe_2O_4$ spinel ferrite nanoparticles synthesized *via* honey-mediated sol-gel combustion method, *J. Phys. Chem. Solids*, 2017, **110**, 87–99.
68 S. T. Assar, H. F. Abosheiasha and M. K. El Nimr, Study of the dielectric behavior of Co–Ni–Li nanoferrites, *J. Magn. Magn. Mater.*, 2014, **350**, 12–18.
69 M. Hashim, S. Kumar, S. Ali, B. H. Koo and H. Chung, Ravi Kumar, Structural, magnetic and electrical properties of Al^{3+} substituted Ni–Zn ferrite nanoparticles, *J. Alloys Compd.*, 2012, **511**, 107–114.
70 S. Narayanan, A. K. Baral and V. Thangadurai, Dielectric characteristics of fast Li ion conducting garnet-type $Li_{5+2x}La_3Nb_{2-x}Y_xO_{12}$ (x = 0.25, 0.5 and 0.75), *Phys. Chem. Chem. Phys.*, 2016, **18**, 15418–15426.
71 L. Singh, U. S. Rai, K. Mandal, B. Cheol Sin, S.-I. Lee and Y. Lee, Dielectric, AC-impedance, modulus studies on $0.5BaTiO_3 \cdot 0.5CaCu_3Ti_4O_{12}$ nano-composite ceramic synthesized by one-pot, glycine-assisted nitrate-gel route, *Ceram. Int.*, 2014, **40**, 10073–10083.

